

Received June 4, 2018, accepted August 22, 2018. Date of publication xxxx 00, 0000, date of current version xxxx 00, 0000.

Digital Object Identifier 10.1109/ACCESS.2018.2868066

Aeromechanic Models for Flapping-Wing Robots With Passive Hinges in the Presence of Frontal Winds

ZHIWEI LI^{ID}, (Student Member, IEEE), SOMPOL SUNTHARASANTIC, SONGNAN BAI, AND PAKPONG CHIRARATTANANON^{ID}, (Member, IEEE)

Department of Mechanical and Biomedical Engineering, City University of Hong Kong, Hong Kong

Corresponding author: Pakpong Chirarattananon (pakpong.c@cityu.edu.hk)

This work was supported by the Research Grant Council of Hong Kong Special Administrative Region, China (project no. CityU-21211315).

ABSTRACT Following the emergence of small flight-capable flapping-wing micro air vehicles, efforts toward autonomous outdoor operations of these small robots outside controlled laboratory conditions have been made. For the robots to overcome wind disturbances, it necessitates better insights into the interaction between the aerodynamics of flapping wings in the presence of winds and the robot's actuation system. In this paper, we consider the effects of constant frontal wind on a direct-drive flapping wing robot with passively rotating hinges and a compliant transmission. A simplified quasi-steady model that encapsulates the effects of frontal wind on aerodynamic forces is proposed. The model facilitates the calculation of periodic aerodynamic forces from nominal flapping kinematics. When combined with the dynamics of the actuation system, we are able to predict the lift force generated by the robot from the driving signals, without direct measurements of the flapping kinematics or the angle of attack. The proposed framework was experimentally verified on a flapping-wing robot prototype with a single wingspan of 76 mm. The results reveal up to 40% increases in lift when the robot was subject to 2.5 m/s horizontal winds. An analysis of the frequency response of the system is also provided to explain the resonance principles of the robot in the presence of frontal winds.

INDEX TERMS Flapping-wing robot, frontal wind, passive hinges, quasi-steady aerodynamics.

I. INTRODUCTION

Intriguing aerial agility of flies and other insects alike has long attracted interests from scientists and engineers. Relying on the reciprocating wing motion, these small flying creatures are capable of complex maneuvers unmatched by any man-made machines. To date, substantial achievements in the understanding of aerodynamics, biomechanics, and flapping flight of insects and hummingbirds have been made [1]–[3]. Together with the technological advancement in robotics [4], a number of flight-capable flapping-wing robots have been developed, ranging from sub-gram piezoelectric actuator driven microrobots [5], [6], centimeter-scale prototypes [7]–[11], to a bird-sized robot with deformable wings [12].

Despite having demonstrated liftoffs or short stable flights, operations of small flapping-wing robots are still predominantly limited to controlled or indoor environments. In order

for insect-scale flapping-wing robots to robustly perform real-world applications, e.g. search and rescue or assisted pollination, they must overcome the effects of external disturbances such as wind gusts. This necessitates better understanding of complex interactions between aerodynamics at small Reynolds number ($Re \sim 10^4$), the mechanics of flapping wings, flight stability, and the dynamics of the robot's actuation system.

In terms of aerodynamics, several studies investigate how gusts affect the performance of flapping flight [13], [14]. Computational methods [15]–[17], as well as particle image velocimetry (PIV) analysis [17]–[19] are often used to identify and explain the unsteady aerodynamic effects, including wing-wake interactions, delayed stall, and stabilized leading edge vortex (LEV). The flow visualization provides a convincing explanation into how the lift generation is altered compared to a regular hovering flight. For instance, at low

advance ratio (J), it was found that LEVs grew more conically, resulting a slight increase in flight forces [19], while the study of free forward flight of cicadas suggests that lift is predominantly generated during the downward stroke [15].

As an alternative or augmentation to numerically solving the Navier–Stokes equations, several researchers employ dynamically-scaled robotic flappers to replicate flapping-wing insects to examine the relationship between the wing kinematics and aerodynamic forces in forward flight [18]–[22]. In [20], a translating and revolving platform was used to measure lift and drag forces for a wing at fixed angle of attacks. In more recent works, the combination of translation and flapping motion is realized [19], [21], [22]. In these studies, variations of quasi-steady models are proposed from empirical data to describe the aerodynamic forces with respect to the flapping kinematics, angle of attack, and the advance ratio. Experimentally, quasi-steady models have been verified sufficiently accurate to describe the observed forces in spite of neglecting the unsteady flow components [22]. Compared to the more comprehensive computational approach, the quasi-steady method offers more tractable solutions suitable for applications in robotics that require further considerations related to actuation dynamics and flight stability.

In flight, forward or lateral motion alters the baseline aerodynamic forces from the hovering condition. The change in lift and drag directly affect the rotational and translational dynamics of a flapping-wing robot. This influences the longitudinal and lateral stability of flapping flight as demonstrated in [11], [15], [19], [21], [23], and [24]. For robotic systems, it is crucial for a flight controller to take into account the additional aerodynamic effects to robustly perform dynamic maneuvers or stabilize in the presence of external gusts. While some control techniques, such as adaptive algorithms, have shown promise [6], capable of stabilizing the insect-scale robot in gusty environments with minimal prior knowledge, it is still advantageous to gain better understanding on the effects of wind disturbance on flapping flight. More accurate models would expand the flight envelope, enhancing the robustness of the flight controller.

The wing kinematics of actual flapping-wing robots, however, are largely impacted by the actuation dynamics of the robot and the disturbances. Small flapping-wing vehicles do not usually incorporate sensors to precisely control the wing kinematics owing to power and weight constraints. Undergoing flapping motion, as the wing encounters additional airflow, the change in instantaneous aerodynamic forces directly affects the force or torque of the actuator. This, in turn, alters the flapping kinematics. In order to correctly predict the aerodynamic effects, as a consequence, it is essential to take into consideration the complete actuation dynamics of the flapping-wing system [9], [25].

In this paper, we aim to investigate the influence of frontal wind on aerodynamic forces experienced by a flapping-wing robot, and to ultimately evaluate the lift generation. The proposed integrated framework takes into account how the

wing kinematics react to the presence of the wind under the given actuation dynamics. More specifically, we study a flapping-wing system with a compliant transmission—the bio-inspired mechanism that enables efficient reciprocating flapping motion [26], and passively rotating wing hinges [27], [28] upon encountering constant frontal gusts.

Flapping-wing robots that utilize elastic components in the transmission are able to store and release mechanical power during each flapping cycle, mimicking the function of insect thoraxes. This renders more efficient operations and minimizes the peak torque required by the actuator. Despite some degree of nonlinearity, the overall actuation systems are capable of resonance [7], [9], [25]. Frictional losses and aerodynamic drags contribute to the dissipation of energy, which determines the flapping amplitude and lift generated by the system.

To evaluate the lift generated by a robot directly from the the driving input and system specifications, therefore, one must determine a steady-state periodic flapping kinematics, of which the resultant aerodynamic forces satisfy the equation describing the dynamics of the actuation system. To achieve this, we modify the quasi-steady models based on previous empirical observations to reduce the model complexity, leading to a more tractable framework. Motivated by the previous work [29] and our preliminary result [30], we assume that the instantaneous wing rotation angle can be determined solely from the instantaneous aerodynamic forces on the wing, neglecting the inertial effect. This allows us to determine the angle of attack of the wing from the flapping amplitude and the wind speed, resulting in the simplified quasi-steady model that is independent of the angle of attack. With the assumption of a sinusoidal flapping motion, approximate, explicit expressions of sinusoidal aerodynamic drag and stroke-averaged lift can be obtained. With the expression of the periodic drag in terms of the flapping amplitude, it is then straightforward to solve the system dynamics equation for the flapping amplitude corresponding to a given driving signal. In short, we are able to predict the flapping amplitude and lift generated by the robot, relying only on the driving signal, the frontal wind speed, and the knowledge of crucial system parameters. Compared to traditional methods that requires solving the coupled aerodynamic and mechanical system models or measurements of the wing rotation angle [27], [28], the proposed method offers a simple alternative for robot designers while providing insights into the interaction between the actuation dynamics and aerodynamics. With some simplifying assumptions, our contribution is a simple model with reasonable accuracy for at-scale flapping experiments. That is, the accuracy of the model is sufficient to describe the experimental results from centimeter or millimeter scale flapping robots that are subject to imperfect fabrication and other unaccounted disturbances. Our approach, therefore, cannot be compared with computational methods that offer more rigorous results at the expense of computational cost.

In the next section, we begin with the description of the flapping kinematics, followed by a nonlinear second order

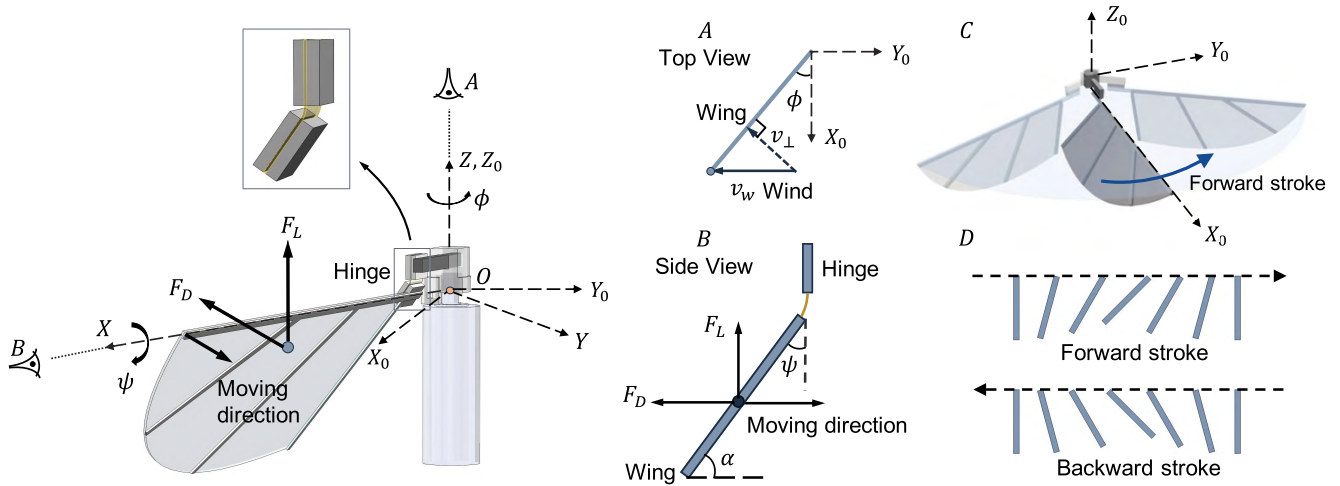


FIGURE 1. Illustration of the Coordinate systems and the flapping kinematics. The flapping angle (ϕ) describes the rotation of the wing about the Z_0 axis. The wing rotation (ψ) presents the rotation of the hinge in the direction along the wing’s leading edge. The wind is assumed to travel along the $-Y$ axis with the speed v_w . (A) and (B) shows the top and side views of the wing in flapping motion. (C) illustrates the wing state in the middle of the forward stroke. (D) highlights the wing rotation during forward and backward strokes.

model of a flapping-wing system capable of resonance. The model outlines the connection between the wing kinematics to the aerodynamic drag and the system input. In section III, a simplified quasi-steady model is proposed. This model eliminates the dependency on the angle of attack from traditional definitions of lift and drag coefficients. Eventually, this allows us to express the aerodynamic drag in the system equation in terms of the flapping amplitude and the frontal wind speed only. Section IV consolidates the results from the two section and offers additional analysis on the resonance properties of the flapping-wing system when the robot with flexural wing hinges is subject to frontal wind. Then, bench-top experiments were performed on a centimeter-scale single-wing flapper with a custom wind generator to verify the proposed framework, including the simplified quasi-steady model and the system model. The tests were carried out on a DC motor-driven robot half with a wing semi-span of 7.6 cm with the flapping conditions corresponding to $Re \sim 4 \times 10^4$ at different advance ratios from 0 to ~ 0.33 . The results are analyzed. The conclusion and further discussion on the proposed method and existing methods are provided in section VII.

II. DESCRIPTIONS OF DIRECT-DRIVE FLAPPING-WING SYSTEMS

A. FLAPPING KINEMATICS

To describe the wing kinematics, we define the inertial reference frame $X_0Y_0Z_0$ and the wing-attached frame XYZ as shown in figure 1. The Z axis of the wing-attached frame coincides with the Z_0 axis, and the leading edge of the wing is parallel to the X axis. The flapping motion, with no stroke plane deviation, is described by the stroke angle ϕ that represents the rotation from X_0 and X about the Z_0 axis. During the flapping motion, the aerodynamic forces induce a passive rotation about the wing hinge [28], [31], causing the angle of

attack (α) to deviate from its nominal angle of 90° . We define the wing pitch rotation angle (ψ) as the rotation of the wing about the X axis such that $\psi = \frac{\pi}{2} - \alpha$. For a sinusoidal flapping motion with an angular frequency $\omega = 2\pi f$, the stroke angle is described by

$$\phi(t) = \phi_1 + \phi_0 \sin \omega t, \quad (1)$$

where ϕ_1 is the mid-stroke position and ϕ_0 is the flapping amplitude. Without loss of generality, we assume a constant wind disturbance of speed v_w in the $-Y_0$ direction. The wind speed in the projected direction perpendicular to the leading edge of the wing (v_{\perp}) is, therefore, $v_{\perp} = v_w \cos \phi$. In this work, we limit the scope to the case of frontal winds. That is, the wind direction is perpendicular to the mid-stroke position, or $\phi_1 = 0$.

B. FLAPPING-WING ACTUATION SYSTEMS WITH RESONANCE

Dipteran insects achieve high wingbeat frequencies in excess of the limit of pure neural activation of flight muscles with the help of the resonance oscillations of the thorax [32]. Similarly, several flapping-wing robots incorporate compliant transmission to replicate the resonance observed in insects to produce efficient reciprocating wing motion. The compliant mechanisms generally contain an elastic component that has an ability to store and release energy during the flapping cycle [26]. In such cases, the wing stroke dynamics are captured by a second-order lumped model in the form:

$$J_m \ddot{\phi} + B_1 \dot{\phi} + K_s \phi + \tau_{aero} = K_u u, \quad (2)$$

where J_m is the moment of inertia, B_1 is an effective linear damping coefficient, K_s is the parameter for the linear torsional stiffness, u is the dimensionless input signal, K_u is the input gain, and τ_{aero} is the aerodynamic damping torque on the wing as it flaps, approximately proportional to $|\dot{\phi}| \dot{\phi}$.

Models similar to equation (2) have been employed to describe the dynamics of a millimeter-scale microrobot driven by a piezoelectric actuator [25], and motor-driven centimeter-scale robots [9], [33]. The inertia term includes the wing inertia as well as other moving parts such as the actuator and transmission. The linear damping is due to the frictional losses in the mechanism and actuation. The stiffness parameter is primarily contributed by the piezoelectric cantilever beam for the robot in [25], or by the addition of a torsional spring for the robots in [9], [33] and our robot. Readers are referred to respective references for comprehensive descriptions of J_m , B_1 , and K_s .

According to previous research and our observation, when driven by sinusoidal voltage inputs, flapping-wing systems often exhibit highly sinusoidal flapping trajectories of the same frequency: $\phi(t) = \phi_0 \sin \omega t$. This is because, apart from the aerodynamic torque (τ_{aero}), the system in equation 2 is linear. When driven by a sinusoidal input, the resultant flapping angle is sinusoidal. The aerodynamic torque term can be regarded as a combination of many sinusoidal components with the dominant term corresponding to the driving frequency and other higher harmonic components. As a second-order system, higher harmonic components are largely attenuated, resulting in a highly sinusoidal flapping stroke. In other words, from the system point of view, only the primary sinusoidal component of τ_{aero} directly affects the flapping amplitude. For this reason, several studies have employed the approximation that the aerodynamic damping torque is proportional to $\dot{\phi}$ by some function $f(\cdot)$ as $\tau_{aero} \approx f(\phi, \dot{\phi})\dot{\phi}$ to facilitate the analysis. For instance, Finio et al. opted to linearized the drag using $f(\cdot) \propto \phi_0$ to always overestimate the actual drag [25], in [7], $f(\cdot)$ was chosen as $f(\cdot) = \frac{3}{8}\pi\omega\phi_0$ to match the stroke-averaged power. While such approaches simplify the system analysis, the system described by equation (2) remains nonlinear. In the following sections, we show that, with a balanced torque assumption [29], [30], how a quasi-steady model can be modified to provide an approximate, analytic expression of $f(\cdot)$ as $f(\phi_0, \omega, v_w)$, which includes the scenario where there exists an influence from frontal gusts (v_w) on a flapping wing. Moreover, the derived model also predicts the lift generated by the flapping wing in the presence of frontal winds.

III. QUASI-STEADY AERODYNAMICS AND FLAPPING-WING SYSTEMS WITH PASSIVE HINGES

A. QUASI-STEADY AERODYNAMICS

For a flat wing with the morphology schematically described in figure 2 in a flapping motion, the blade-element method provides a convenient way to compute aerodynamic forces by considering the force component at each chordwise strip along a flapping wing. We let r be the distance along the X axis from the origin of the wing-attached frame, and $c(r)$ describe the chord length at position r . In the flapping motion, the wing undergoes a rotation prescribed by $\phi(t) = \phi_0 \sin \omega t$. Assuming only the normal component of the

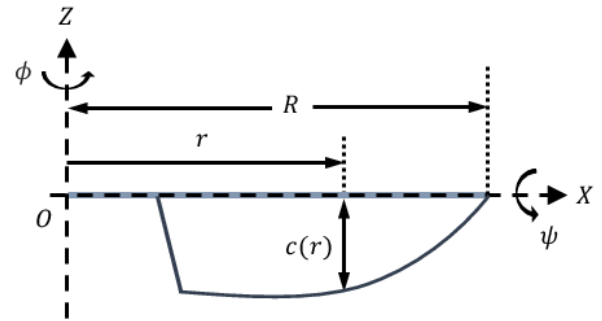


FIGURE 2. Wing morphology parameters: R is the single wingspan, O is wing root and the origin of the wing-attached frame, r is the distance along the X -axis from O , and $c(r)$ denotes the chord length at position r . The flapping angle and the wing rotation are described by ϕ and ψ .

airspeed contributes to aerodynamic forces [34], the instantaneous lift and drag forces produced by the whole wing in the presence of the gust v_w is computed from the sum of all elements according to the quasi-steady model:

$$F_{L,D}(\psi, \dot{\phi}, v_{\perp}) = \frac{1}{2} \rho C_{L,D}(\psi) \int_{r=0}^R \int_{c'=0}^{c(r)} (\dot{\phi}r + v_{\perp})^2 dc' dr, \quad (3)$$

where ρ is the air density, $v_{\perp} = v_w \cos \phi$, is the component of the wind perpendicular to the leading edge of the wing, and $C_{L,D}$ is the lift/drag coefficient, which can be written as functions of the wing's rotation angle [35]:

$$C_L(\psi) = C_{L0} \sin(2\psi) \quad (4)$$

$$C_D(\psi) = C_{D0} + C_{D1} \cos(2\psi). \quad (5)$$

The numerical coefficients ($C_{L0} = 1.8$, $C_{D0} = 1.9$, $C_{D1} = 1.5$) were empirically determined and used for other flapping wings at similar scales [29], [35], [36]. The expression of lift and drag can be further expanded using the definition of a dimensionless radius i^{th} moment of area $\hat{r}_i^i = \int_0^R c(r) r^i dr / AR^i$ [37] as

$$F_{L,D} = \frac{1}{2} \rho C_{L,D}(\psi) A \left(\dot{\phi}^2 R^2 \hat{r}_2^2 + 2\dot{\phi} R \hat{r}_1 v_{\perp} + v_{\perp}^2 \right). \quad (6)$$

Similar to other models for robotics applications [9], [29], [38], other aerodynamic forces such as rotational forces and added mass effects are neglected in this work as they provide secondary effects. In addition, the stroke-averaged values of those terms are typically close to zero (further details provided in the supplementary materials).

B. PASSIVE WING PITCH ROTATION AND EQUILIBRIUM ASSUMPTION

For flapping-wing robots with flexural hinges and thin wings as found in [6], [8], and [29] and our robot, the dynamics of the wing pitch rotation, in the absence of out-of-plane motion, simplifies to [27]

$$I_{xx} \ddot{\psi} = \tau_h + \tau_r + I_{xy} \ddot{\phi} \cos \psi + \frac{1}{2} I_{xx} \dot{\phi}^2 \sin 2\psi, \quad (7)$$

where I_{ij} 's are the elements in the wing's inertia tensor computed about the wing's attached frame in figure 1, and τ_h and τ_r are the moments caused by the elastic hinge and aerodynamic forces respectively. The third term on the right hand side of the equation above is the inertial component contributed by the fact that the rotational axis does not align with the centre of mass of the wing. Gravish and Wood [29] proposed to simplify equation (7) further by neglecting the inertial terms, resulting in the balanced torque condition: $\tau_h + \tau_r = 0$. This assumption is justified for the calculation of aerodynamic forces, as $\dot{\phi}, \dot{\psi} \rightarrow 0$ in the mid-stroke, where aerodynamic forces peak.

The restoring torque generated by the hinge rotation is approximately proportional to the rotational stiffness of the hinge (k_h) such that $\tau_h = -k_h\psi$, whereas the total aerodynamic torque about the X axis (τ_r) can be calculated as the sum of lift and drag elements acting normal to the wing according to figure 1 and equation (3),

$$\tau_h = \frac{1}{2}\rho (C_L \sin \psi + C_D \cos \psi) \int_{r=0}^R \int_{c'=0}^{c(r)} c' (\dot{\phi}r + v_{\perp})^2 dc' dr. \quad (8)$$

By defining

$$F = F_L \sin \psi + F_D \cos \psi, \quad (9)$$

and the chordwise center of pressure

$$c_{ca} = \frac{\int_{r=0}^R \int_{c'=0}^{c(r)} c' (\dot{\phi}r + v_{\perp})^2 dc' dr}{\int_{r=0}^R \int_{c'=0}^{c(r)} (\dot{\phi}r + v_{\perp})^2 dc' dr}, \quad (10)$$

we get $\tau_h = c_{cp}F$ and the assumption of balanced torque becomes $k_h\psi = Fc_{ca}$. Note that this chordwise center of pressure—the location where the aerodynamic forces act on the wing—deviates from the conventional definition that refers to the spanwise center of pressure [38]. In the absence of frontal winds, c_{cp} is constant for a particular wing morphology, regardless of the flapping kinematics:

$$c_{cp}|_{v_{\perp}=0} = \frac{\int_{r=0}^R \int_{c'=0}^{c(r)} c' r^2 dc' dr}{\int_{r=0}^R \int_{c'=0}^{c(r)} r^2 dc' dr}, \quad (11)$$

otherwise, c_{cp} varies with $\dot{\phi}$, complicating the analysis. Nevertheless, we can bound the value of c_{cp} by considering the scenario where $\dot{\phi} \rightarrow 0$ as

$$c_{cp}|_{\dot{\phi}=0} = \frac{\int_{r=0}^R \int_{c'=0}^{c(r)} c' dc' dr}{A}. \quad (12)$$

For the sake of simplicity, it is reasonable to assume a constant c_{cp} that lies between the bounds from equations (11) and (12). Then, according to equation (6), the assumption of balanced torque becomes

$$\frac{1}{2k_h} \rho A c_{cp} (\dot{\phi}^2 R^2 \hat{r}_2^2 + 2\dot{\phi}R\hat{r}_1 v_{\perp} + v_{\perp}^2) = \frac{\psi}{\sin(\psi)C_L(\psi) + \cos(\psi)C_D(\psi)}. \quad (13)$$

It can be seen that equation (13) separates the terms with the wing rotation angle ψ to the right hand side, whereas the left hand side is a dimensionless quantity related to the perceived airspeed. This implies we can determine the wing pitch angle from the current airspeed of the wing only. In the absence of the frontal gust, this reduces to a simpler form we previously presented in [30]. From here, we let x represent the quantity on the left hand side of the equation (13), which will be referred to as the normalized squared airspeed. It follows that equation (13) can be numerically solved for ψ as $\psi = f^{-1}(x)$. The use of the dimensionless quantity x enables us to generalize the framework presented below to a broad range of flapping-wing robots with passively rotating hinges.

C. APPROXIMATE WING ROTATION ANGLE AND INSTANT AERODYNAMIC FORCES

While it is possible to numerically calculate ψ from x from equation (13), it is desirable to obtain an explicit solution to facilitate further analysis. Previously, we demonstrated that a simple 2nd-order polynomial fit, $\psi = a_1x + a_2x^2$ with $a_1 = 3.54$ and $a_2 = -3.04$, provides a highly accurate estimate of ψ with respect to the direct solution from equation (13) for $\psi < \pi/3$, resulting in the maximum error $|\psi - \hat{\psi}|$ of 0.02 rad [30]. The comparison is illustrated in figure 3(a). The upper limit of $\psi = \pi/3$, corresponding to $x = 0.54$, is suitable for flapping-wing robots designed to avoid over-rotation, which may cause a significant reduction in lift.

Major considerations for a flapping-wing robot, nevertheless, are not the wing rotation angle, but the aerodynamic forces, or lift and drag. Using the definition of normalized squared airspeed (x) and the fact that ψ is a function of x under the assumption of balanced torque, we re-write equation (6) as

$$F_{L,D} = \frac{k_h}{c_{cp}} x C_{L,D}(x), \quad (14)$$

which motivates us to directly approximate $C_{L,D}$ as polynomial functions of x . More specifically, we define

$$\begin{aligned} \hat{C}_L &= C_{L0} (\alpha_1 x + \alpha_2 x^2 + \alpha_3 x^3), \quad \text{and} \\ \hat{C}_D &= C_{D0} + C_{D1} (\beta_0 + \beta_1 x + \beta_2 x^2), \end{aligned} \quad (15)$$

where α_i 's and β_i 's are numerical coefficients, listed in table (1). Figure 3(b) compares the estimated lift and drag coefficients with the ones calculated from equation (4) as a function of x . The result reveals that three coefficients are sufficient to approximate $C_{L,D}$. Moreover, this allows us to directly estimate the aerodynamic forces as

$$\hat{F}_{L,D}(x) = \frac{k_h}{c_{cp}} x \hat{C}_{L,D}(x). \quad (16)$$

As demonstrated in figure 3(c), the estimated aerodynamic forces only slightly deviate from the numerical model. The maximum discrepancy of less than 5% is only seen at large airspeed ($x = 0.7$).

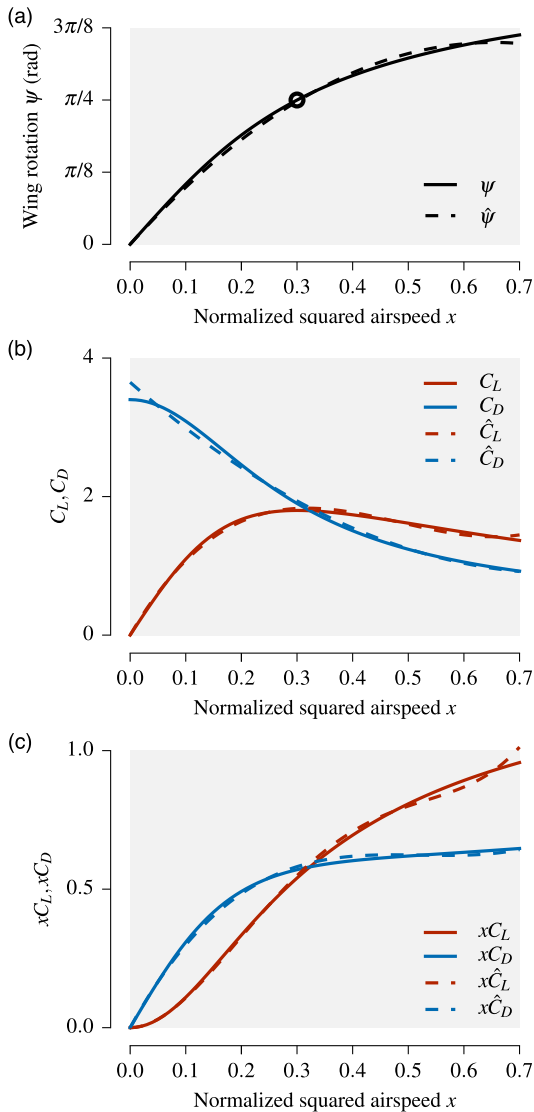


FIGURE 3. Model predictions of the wing rotation angle, lift and drag coefficients, and lift and drag forces with respect to the normalized square airspeed. (a) The wing rotation angle calculated directly from the numerical model (solid line) from equation (13) and from the polynomial approximation (dashed line): $\hat{\psi} = \alpha_1 x + \alpha_2 x^2$. The circular marker indicates the optimal rotation angle $\psi = 45^\circ$ when $x = 0.30$. (b) The lift and drag coefficients obtained from the numerical models (solid lines) and the proposed polynomial functions (dashed lines). (c) The corresponding normalized lift and drag forces based on the coefficients in (b).

D. LIFT AND DRAG WITH PERIODIC FLAPPING KINEMATICS

In the development of a flapping-wing robot, we are interested in the stroke-averaged lift generated when the robot is driven by a sinusoidal input such that the flapping angle is approximately described by $\phi = \phi_0 \sin \omega t$. In the meantime, it is important to take into consideration the drag force, particularly, the primary component of the drag corresponding to the flapping frequency as it plays a critical role in determining the flapping amplitude as captured by dynamics of the system according to equation (2).

TABLE 1. Aerodynamic coefficients.

Coefficients	Values
C_{L0}	1.8
C_{D0}	1.9
C_{D1}	1.5
a_1	3.54
a_2	-3.04
α_1	7.64
α_2	-17.85
α_3	12.25
β_0	1.17
β_1	-4.71
β_2	3.01

In order to take into account the periodicity of the aerodynamic forces while retaining the tractability of the model, we propose to make two simplifying approximations on x from equation (13). First, we seek to eliminate the time-dependence of $v_\perp = v_w \cos \phi = v_w \cos(\phi_0 \sin \omega t)$. This is achieved by approximating v_\perp using its stroke-averaged value

$$v_\perp \approx \frac{1}{T} \int_{t=0}^{t=T} v_w \cos(\phi_0 \sin \omega t) dt = v_w J_0(\phi_0), \quad (17)$$

$$= \bar{v}_\perp$$

where $J_0(\cdot)$ is the zero-order Bessel function of the first kind. The value of \bar{v}_\perp depends not only on v_w , but also ϕ_0 . In fact, for the range of realistic flapping amplitude (for example, $\phi_0 < 3\pi/4$), $J_0(\phi_0)$ is a decreasing function. The expression implies that the effect of the frontal wind becomes less important at larger stroke amplitude. This is owing to the wing spending proportionally shorter time in the orientation perpendicular to the wind direction.

Next, we employ a single dimensionless number, \hat{r} , to estimate \hat{r}_1 and \hat{r}_2 such that $\hat{r} \approx \hat{r}_1, \hat{r}_2$. Both simplifications lead to

$$x \approx \frac{1}{2k_h} \rho A c_{cp} (\dot{\phi} R \hat{r} + \bar{v}_\perp)^2. \quad (18)$$

For simplicity, we define $v_\phi = \omega \phi_0 R \hat{r}$ to denote the maximum flapping speed. It follows that, for a sinusoidal flapping kinematics, $\phi = \phi_0 \sin \omega t$, it is straightforward to analytically evaluate stroke-averaged values (denoted by $\langle \cdot \rangle$) of x^i . For instance,

$$\langle x \rangle = \frac{1}{2k_h} \rho A c_{cp} \left(\frac{1}{2} v_\phi^2 + \bar{v}_\perp^2 \right),$$

$$\langle x^2 \rangle = \left(\frac{1}{2k_h} \rho A c_{cp} \right)^2 \left(\frac{3}{8} v_\phi^2 + 3 v_\phi^2 \bar{v}_\perp^2 + \bar{v}_\perp^4 \right), \quad (19)$$

and so on. The time-averaged lift is, therefore, derived from equations (15) and (16) as

$$\langle \hat{F}_L \rangle = \frac{k_h}{c_{cp}} C_{L0} (\alpha_1 \langle x^2 \rangle + \alpha_2 \langle x^3 \rangle + \alpha_3 \langle x^4 \rangle). \quad (20)$$

The drag force has a first-order effect on the aerodynamic torque (τ_{aero}), which directly influences the flapping amplitude of the robot as outlined by the system model in equation (2). Since only the first harmonic component of the

torque directly affects the flapping amplitude, we are only interested in this primary component. This does not, in any way, mean that the aerodynamic drag is approximately sinusoidal.

To begin, we take into account the direction of the force during the flapping period. In other words, we express \hat{F}_D as

$$\hat{F}_D = -\frac{k_h}{c_{cp}} (\dot{\phi}R\hat{r} + \bar{v}_\perp) |\dot{\phi}R\hat{r} + \bar{v}_\perp| \hat{C}_D(x). \quad (21)$$

Next, we aim to employ the Fourier series approximation to compute the magnitude of the first harmonic component of \hat{F}_D from $\frac{2}{T} \int_{t=0}^{t=T} \hat{F}_D \cos \omega t dt$. To work around the presence of the absolute term in equation (21), we use the fact that, at relatively small v_w , the sign of the $(\dot{\phi}R\hat{r} + \bar{v}_\perp)$ term mostly coincides with the sign of $\cos \omega t$. The exception only occurs when $(\dot{\phi}R\hat{r} + \bar{v}_\perp) \approx 0$, which is unimportant as the corresponding aerodynamic drag also approaches zero. This motivates us to move the absolute sign to the $\cos \omega t$ term to yield the following:

$$\begin{aligned} \left[\hat{F}_D \right] &\approx -\frac{2}{T} \int_{t=0}^{t=T} \frac{k_h}{c_{cp}} \\ &\cdot \left[C_{D0}x + C_{D1} (\beta_0x + \beta_1x^2 + \beta_2x^3) \right] |\cos \omega t| dt \\ &= -\frac{k_h}{c_{cp}} \left[C_{D0} \llbracket x \rrbracket + C_{D1} \right. \\ &\cdot \left. \left(\beta_0 \llbracket x \rrbracket + \beta_1 \llbracket x^2 \rrbracket + \beta_2 \llbracket x^3 \rrbracket \right) \right], \quad (22) \end{aligned}$$

where we have introduced the notation $\llbracket \cdot \rrbracket = -\frac{2}{T} \int_{t=0}^{t=T} |\cos \omega t| dt$ to represent the approximate amplitude of the first harmonic component. The proposed method enables us to estimate \hat{F}_D as $\llbracket \hat{F}_D \rrbracket \cos \omega t$ using the analytical expression of $\llbracket x^i \rrbracket$, of which some examples are provided as follows

$$\begin{aligned} \llbracket x \rrbracket &= \frac{1}{2k_h} \rho A c_{cp} \left(\frac{8}{3\pi} v_\phi^2 + \frac{4}{\pi} \bar{v}_\perp^2 \right), \\ \llbracket x^2 \rrbracket &= \left(\frac{1}{2k_h} \rho A c_{cp} \right)^2 \left(\frac{32}{15\pi} v_\phi^4 + \frac{16}{\pi} v_\phi^2 \bar{v}_\perp^2 + \frac{4}{\pi} \bar{v}_\perp^4 \right). \quad (23) \end{aligned}$$

The numerical predictions of lift and drag forces are illustrated in figure 4. Overall, the numerical models ($\langle F_L \rangle$, $\llbracket F_D \rrbracket$, points) and polynomial models ($\langle \hat{F}_L \rangle$, $\llbracket \hat{F}_D \rrbracket$, solid lines) provide good agreements. Figure 4(a) and (c) show how the stroke-averaged lift varies when v_ϕ and \bar{v}_\perp change. The lift enhancement can be as large as 40% for modest values of \bar{v}_\perp . The numerical models suggest that the contribution from v_\perp only significantly affects the lift at intermediate values of v_ϕ . This is likely because the wind becomes relatively unimportant at larger flapping amplitude and faster wing speed.

The predictions of the drag amplitude reveal an interesting phenomenon. As seen from figure 4(b), at small v_ϕ , the introduction of frontal wind increases the aerodynamic drag. However, the trend reverses when $\frac{1}{2k_h} \rho A c_{cp} v_\phi^2 > 1.8$. Above this threshold, the flapping wing experiences an increase in lift

and a reduction in drag—a highly desirable condition for the robot.

To sum up, in this section, we have proposed to neglect the inertial terms in the consideration of wing pitch dynamics. This balanced torque assumption allows us to exploit polynomial functions to analytically approximate instantaneous lift and drag forces experienced by a flapping wing in the presence of constant frontal wind. The aerodynamic forces can be further examined to obtain an expression of the stroke-averaged lift and the first-order sinusoidal approximation of the drag. All these quantities can be computed directly in a single step without directly solving the equations of motion for steady-state solutions as traditionally required.

IV. DIRECT-DRIVE FLAPPING-WING SYSTEMS WITH QUASI-STEADY AERODYNAMIC MODELS

A. COMPLETE SYSTEM MODEL

The estimated aerodynamic drag can be incorporated into the system model described by equation (2). To achieve that, we assume that the aerodynamic torque seen by the motor is proportional to the total drag acting on the wing, $\tau_{aero} = r_{cp} F_D$, with r_{cp} representing the spanwise location of the center of pressure [38]. The dynamics of the robot actuation becomes

$$J_m \ddot{\phi} + B_1 \dot{\phi} + K_s \phi + r_{cp} F_D = K_u u. \quad (24)$$

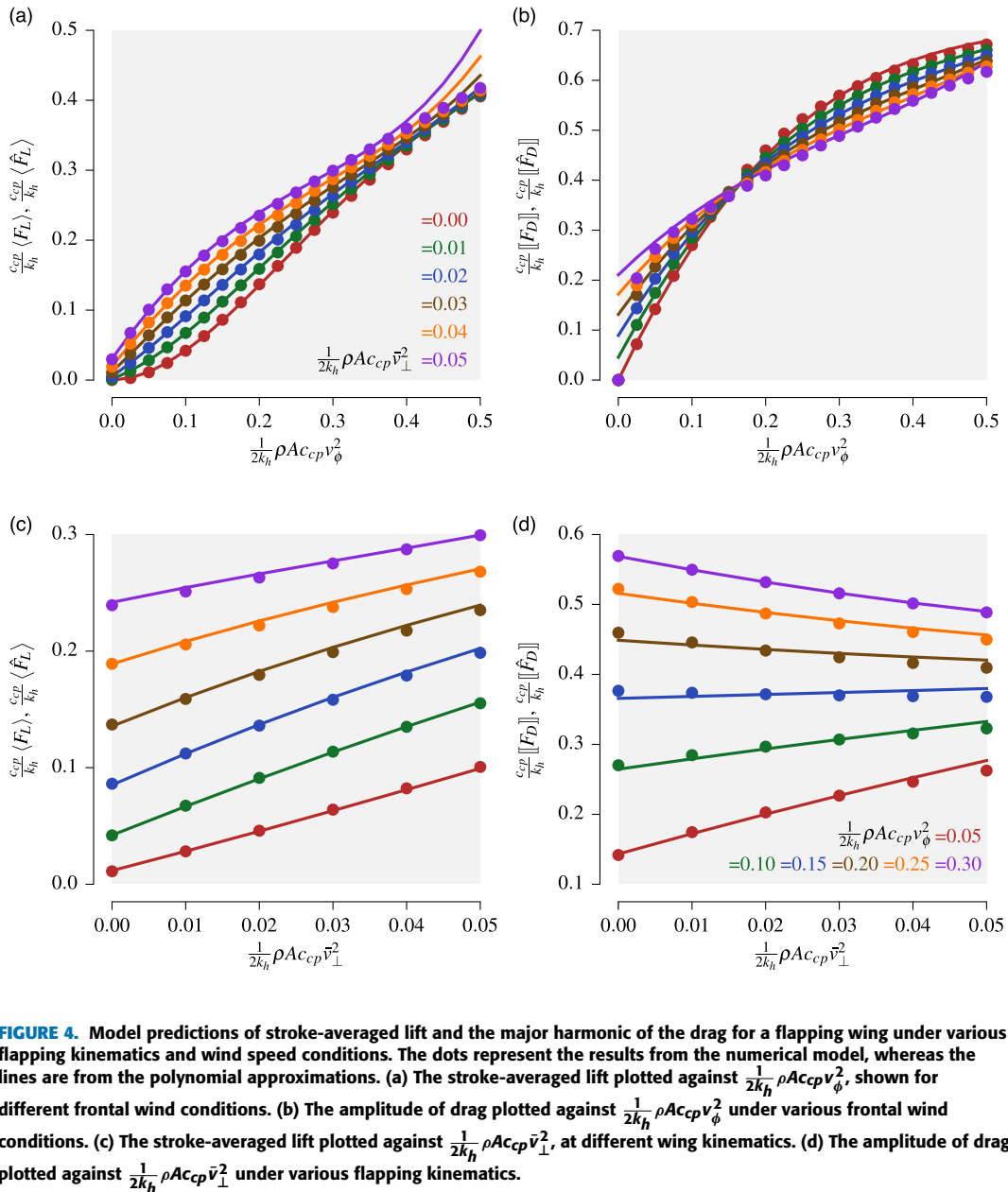
For a sinusoidal input $u = u_0 \sin(\omega t + \theta)$ (for some θ , depending on the phase response of the system) with the corresponding sinusoidal wing trajectory prescribed by $\phi(t) = \phi_0 \sin \omega t$ as assumed previously, the derivation in Section III-D suggests that $F_D \approx \llbracket \hat{F}_D \rrbracket \cos \omega t$. After substituting $\phi(t)$ and F_D into equation (24), we obtain the steady-state response of the system:

$$\left(K_s - J \omega^2 \right)^2 \phi_0^2 + \left(B_1 \omega \phi_0 + r_{cp} \llbracket \hat{F}_D \rrbracket \right)^2 = K_u^2 u_0^2. \quad (25)$$

With the knowledge of the physical parameters of the robot, solving the equation above directly allows us to compute the flapping amplitude, ϕ_0 , using only the input amplitude, the driving frequency, and the frontal wind speed in a single step. Once the flapping amplitude is determined, the lift force can be predicted using equation (20). In other words, with a few simple analytical expressions, we can predict the flapping amplitude and lift generated by a flapping-wing robot with frontal gusts directly from the driving input.

B. RESONANCE ANALYSIS

Despite the inherently nonlinear dynamics of flapping-wing robots, several direct-drive robots exhibit the system resonance, demonstrating peak flapping amplitudes or maximum lifts when driven at particular frequencies [5], [7], [9], [33]. Previously, it has been theoretically shown and experimentally verified that, for a flapping-wing robot with freely rotating hinges and wing stoppers, there exists a peak frequency where the flapping amplitude is largest, and a slightly higher



natural frequency that the robot achieves the maximum flapping velocity and lift [9]. Herein, we show that, through our lift and drag approximations from Section III, to the first order, a direct drive system with flexural wing hinges under the influence of constant frontal wind also possesses a natural frequency. At this natural frequency, the flapping velocity is maximized, nevertheless, lift is only largest at the natural frequency when the frontal wind is absent.

To begin, we let ω_0 denote the natural frequency, which is defined as the flapping frequency that maximizes the flapping speed (v_ϕ). To determine ω_0 , we write equation (25) in terms of v_ϕ and differentiate it with respect to ω . The term $d \left[\hat{F}_D \right] / d\omega$ can be computed using the chain rule as

$\left(d \left[\hat{F}_D \right] / dv_\phi \right) \cdot (dv_\phi / d\omega)$. At ω_0 , $dv_\phi / d\omega = 0$ and we obtain the solution $\omega_0 = \sqrt{K_s / J_m}$, regardless whether there exists a frontal wind. At this natural frequency, the flapping speed is highest, similar to a flapping-wing system with freely rotating hinges and wing stoppers [9].

From this point, to evaluate the frequency that provides the maximum lift, we examine the approximate expression of stroke-averaged lift in equation (20) and the plot of lift in figure 4(a). In the absence of the frontal wind ($\bar{v}_\perp = 0$), lift is a monotonously increasing function of the flapping speed (v_ϕ). As a consequence, the condition for the maximum lift production coincides with that of the highest flapping speed. In other words, the model predicts lift to

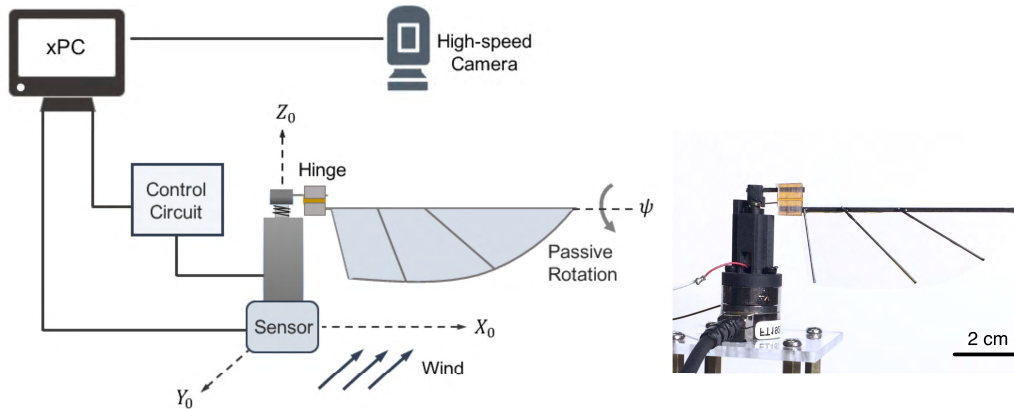


FIGURE 5. The experimental setup. The robot is mounted on the force sensor next to the wind generator (not shown). The camera captures the flapping motion for tracking the flapping amplitude.

be maximized at the natural frequency in the absence of winds.

When $\bar{v}_\perp \neq 0$, lift is no longer guaranteed a monotonous increasing function of v_ϕ as \bar{v}_\perp is not independent of ϕ_0 . With the analytical expression of $\langle \hat{F}_L \rangle$, it is still feasible to evaluate the equation that enables us to determine the flapping frequency that maximizes the lift when the frontal wind is present. Nevertheless, the expression becomes sophisticated and the solution becomes a function of the wind speed v_w and the input amplitude. It is more reasonable to resort to numerical solutions for the task. Similarly, it is also possible to find the peak frequency, where the flapping amplitude is maximized, using the same method. However, we omit the detail due to the lack of a simple analytical solution.

V. FLAPPING EXPERIMENTS

A. FLAPPING-WING ROBOT

To verify the proposed framework, flapping experiments were conducted on a centimeter scale single-wing flapper. The robot consists of a motor, a torsional spring, a hinge, and a wing. The spring confines the rotational movement of the wing to the mechanical ground, acting as an elastic element to create the resonance similar to the system described in [9]. The motor (BO-P1B, Vigor Precision) with the stall torque of 1.765 N·mm was selected as an actuator. In addition to the rotation of the motor shaft that induces the flapping angle (ϕ), the wing also rotates passively along its leading-edge by the angle (ψ) thanks to the flexural wing hinge.

The wing frame is made of carbon fiber spars and adhered to a thin polyester membrane layer (Mylar, $6\mu\text{m}$). An assemble jig is used for the alignment of the carbon fiber frame to ensure consistent results. The wing used on the flapping-wing robot has an area of 1127 mm² with the total length $R = 76$ mm as listed in Table 2. The coupler connecting the wing and the motor shaft is 3D printed from stereolithography resin (Black Resin, Formlabs Form 2).

B. EXPERIMENTAL SETUP

Figure 5 depicts the experimental setup. The robot was mounted on the multi-axis force/torque sensor (Nano17, ATI)

TABLE 2. Robot parameters.

Variables	Values	Units
Wing parameters		
R	76	mm
A	1127	mm ²
$c_{cp} _{v_\perp=0}$	9.61	mm
$c_{cp} _{v_\phi=0}$	10.07	mm
c_{cp}	9.7	mm
\hat{r}_1	0.58	-
\hat{r}_2	0.61	-
\hat{r}	0.73	-
k_h	0.66	N·mm·rad ⁻¹
mass	132	mg
System parameters		
J_m/K_u	6.33×10^{-5}	s ²
B_1/K_u	3.14×10^{-2}	s
K_s/K_u	0.67	-
r_{cp}/K_u	7.93	N ⁻¹
ω_0	$2\pi \times 16.4$	rad·s ⁻¹

with the sensor's Z axis aligned with the lift direction. The force and torque data from the sensor were recorded using the xPC system (Mathworks) at 5 kHz, together with the current and voltage data of the motor. We take the force measurements from along Z axis of the sensor as the lift generated by the robot. From our sensor calibration tests (see the electronic supplementary materials), we achieve the force resolution of ~ 0.5 mN when the sensor is thermally insulated.

A high-speed camera (MIKROTRON MotionBLITZ EoSens Mini 2) is mounted above the wing to capture the flapping stroke angle at 1440 frames per second. The camera is triggered by the xPC system, allowing the driving signal, the force measurements, and the wing kinematics to be synchronized. A customized wind generator was made from an array of 4×5 12-V DC cooling fans with an aluminum flow straightener for providing frontal winds for the flapping-wing robot (see details in the supplementary materials). In steady state, the wind generator is able to consistently produce wind with the speed ranging from $(0.5 - 2.5) \pm 0.05$ m·s⁻¹ depending on the command signal. With the small temporal variation

in wind speed ($\pm 0.05 \text{ m}\cdot\text{s}^{-1}$), we treat the wind speed as a constant parameter for each flapping experiment.

C. ESTIMATION OF PARAMETERS

1) SYSTEM PARAMETERS

To identify some system parameters that determine the system's response according to equations (2) and (24), we manufactured a single-wing flapper consisting of a wing driver and wing spars without the membrane. Without the membrane, the wing experiences negligible aerodynamic forces in the flapping motion and the dynamics of the robot reduces to that of a second-order linear system:

$$\frac{J_m}{K_u} \ddot{\phi} + \frac{B_1}{K_u} \dot{\phi} + \frac{K_s}{K_u} \phi = u \quad (26)$$

With a sinusoidal input in the standard form $u(t) = (u_0 \sin \omega t + \theta)$, the flapping amplitude is related to the driving frequency and amplitude according to

$$\left(\frac{K_s}{K_u} - \frac{J}{K_u} \omega^2\right)^2 + \left(\frac{B_1}{K_u} \omega\right)^2 = \left(\frac{u_0}{\phi_0}\right)^2. \quad (27)$$

We performed a simple system identification experiment by driving the membrane-less flapper with sinusoidal signals with different frequencies, ranging from 14 to 20 Hz. The experiments were carried out at two signal amplitudes ($u_0 = 0.30, 0.35$). The high-speed camera captured the wing kinematics. The flapping amplitudes extracted from the video footages are plotted against the driving frequency as points in figure 6. With seven different operating frequencies and two signal amplitudes, 14 equations derived from equation (27) were used to compute the values of J_m/K_u , B_1/K_u , and K_s/K_u using the method of least-squares. These model parameters are listed in table 2. The identified model parameters suggest the natural frequency ω_0 of $2\pi \times 16.4 \text{ rad/s}$. At this frequency, the robot with the wing membrane is anticipated to produce the maximum lift. The peak frequency, at which the largest flapping amplitude is expected, on the other hand, is approximately 15.5 Hz according to figure 6. The fitted model, also shown in figure 6, reveals a good fit to the experimental data. This verifies that the linear model is sufficiently accurate to capture the dynamics of the actuation system when aerodynamic forces are excluded.

2) WING HINGE STIFFNESS

The passively rotating hinge is manufactured resembling the design in [27]. The hinge is made from five layers of materials by sandwiching a flexible material between rigid structures. The top and bottom layers are symmetrically aligned stereolithography resin with the thickness of $500 \mu\text{m}$. The middle layer is a flexural material (Kapton, Dupont, 200HN). Two pressure sensitive adhesive layers (EL-92892, Adhesives Research) are used to bond the flexural material and the resin layers. When torque applied, it results in a bending along the middle portion of the flexure. The torques required are plotted against the rotation angle in figure. 7, giving the estimated

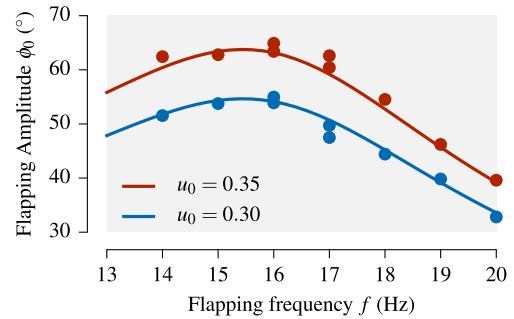


FIGURE 6. System identification results. The plot shows the flapping amplitudes of the membrane-deprived robot when subject to driving signals with different frequencies at two input amplitudes. The lines represent the anticipated response of the identified linear second order model.

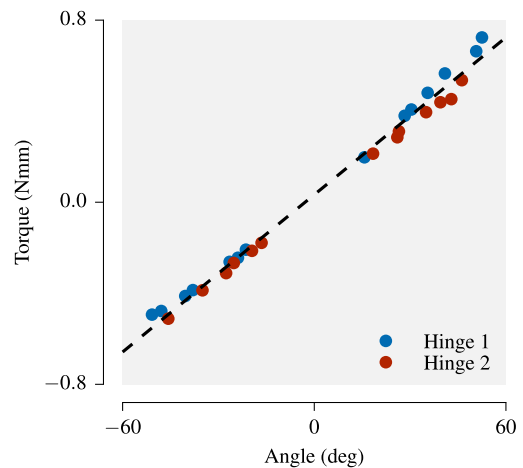


FIGURE 7. The results of the hinge stiffness tests. The torque measurements verify that the torsional stiffness is approximately linear.

rotational stiffness of $0.66 \text{ Nmm}\cdot\text{rad}^{-1}$. Further details of the hinge stiffness test are given in the supplementary materials.

Theoretically, the rotational stiffness of the hinge can be approximated by that of a linear elastic beam deforming under an external moment as $k_h = \frac{Et^3w}{12l}$, where E represents the Young's Modulus of the flexural material with thickness t . w and l represents the width and the length of the hinge gap. The hinge used in the experiments is made from Kapton with $E = 2.5 \text{ GPa}$, $t = 75 \mu\text{m}$, $w = 6.7 \text{ mm}$, and $l = 0.7 \text{ mm}$, which results in a theoretical stiffness of $0.84 \text{ Nmm}\cdot\text{rad}^{-1}$. The small discrepancy between the measurement and the theoretical values could be due to the softening effect or the strong dependent on the thickness t , which may locally vary in the actual material.

D. FLAPPING EXPERIMENTS

The flapping experiments were conducted by driving the DC motor with sinusoidal inputs with the amplitude from 4 V to 6 V ($u_0 = 0.4-0.6$), at different frequencies from 15 Hz to 21 Hz. The frontal wind speed varies from 0 to $2.5 \text{ m}\cdot\text{s}^{-1}$ with an increment of $0.5 \text{ m}\cdot\text{s}^{-1}$. The force and torque data along

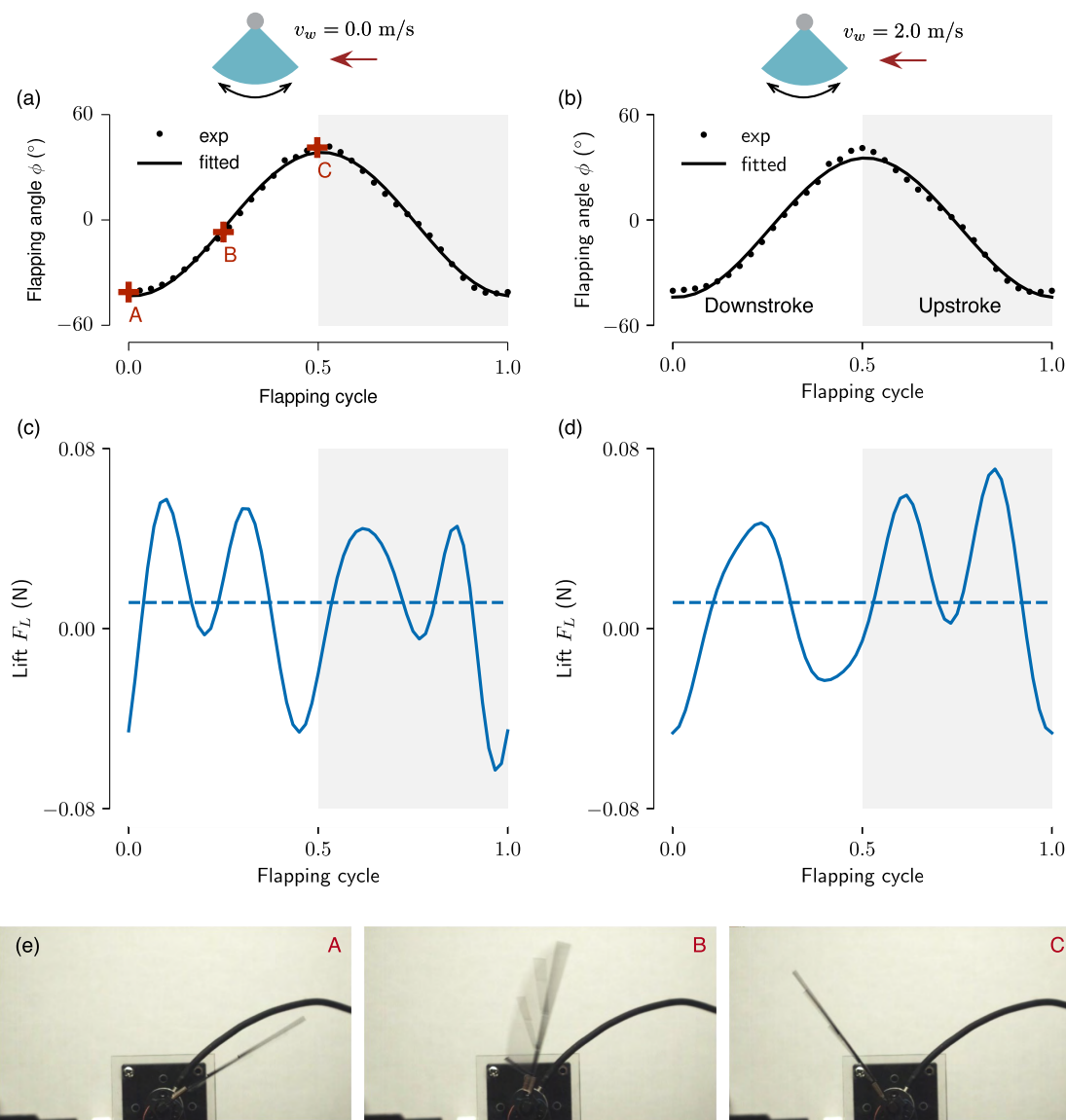


FIGURE 8. Measurements from the flapping experiments when the robot was driven with $u_0 = 0.50$ at the flapping frequency of 18 Hz under two frontal wind conditions ($v_w = 0.0, 2.0$ m/s). (a), (b) the measurements of flapping angles taken from the high-speed video (dots) with the sinusoidal fit (lines) in the form $\phi(t) = \phi_0 \sin \omega t$. The red dots, labelled A, B and C, correspond to the frames captured by the high-speed camera in (e). The flapping amplitudes when $v_w = 0.0$ and 2.0 m/s are nearly identical. (c), (d) the instantaneous force measurements from the two flapping conditions. Each line represents the averages of over 30 cycles. The overall stroke-averaged values are indicated by horizontal dashed lines.

the X , Y and Z axis of the sensor were recorded using the xPC system (Mathworks) at 5 kHz, together with the current and voltage of the motor. We performed 105 flapping trials, 56 of which are in the presence of winds. We attempted to minimize the number of experimental trials to avoid possible damage and potential mechanical fatigue of the flexural wing hinge as observed in other robots [39]. The mechanical wear may reduce the hinge stiffness over time, making comparison of measurement results between different trials unreliable.

In each flapping trial, the stroke-averaged lift value was taken from 30-50 flapping cycles. The flapping amplitudes

are obtained from the sinusoidal fit of the flapping angles extracted from 60 image frames. From 107 trials, the dataset covers a reasonable range of flapping amplitude ($\approx 30^\circ - 60^\circ$). The stroke-averaged lift ranges from 7.4 to 23.9 mN, with the average of 14.8 mN. In the absence of frontal wind, the maximum lift of 16.7mN was achieved when the flapping amplitude was 60° as the sinusoidal driving voltage with 6 V amplitude was used. The generated lift and stroke amplitude are comparable to other direct-drive flapping-wing robots with similar sizes [33], [40]. Moreover, there is still room to achieve a higher lift as the input signal can be further amplified.

The Given the wing length of 76 mm and the kinematic viscosity of air (ν), the Reynolds number of our flapping wing robot is

$$Re = (\omega\phi_0 R + v_w) \frac{R}{\nu} \sim 4 \times 10^4, \quad (28)$$

where the maximum advance ratio is found to be

$$J = \frac{v_w}{\omega\phi_0 R} = 0.33. \quad (29)$$

Figure 8(a)-(b) demonstrates the wing kinematics of the robot extracted from the video footage from two trials when the robot was commanded to operate at 18 Hz with the driving amplitude $u_0 = 0.50$. In the first case, figure 8(a), the robot experienced no external gusts, whereas in figure 8(b), it was subject to 2.0-ms^{-1} wind. Comparing the data to their respective fitted wing kinematics in the form $\phi(t) = \phi_0 \sin \omega t$, it can be seen that, the actual wing kinematics are highly sinusoidal for both cases, meeting our assumption in Section III-D. The flapping amplitude, in this case, are generally smaller than those obtained from the identification experiment despite the fact that the robot was subject to larger input amplitudes. This evidently demonstrates the effects of aerodynamic drag on the flapping amplitude as predicted by the model. Furthermore, herein, we do not observe a notable difference in amplitude whether or not the wind is present, suggesting that the presence of the frontal wind only trivially affects the flapping kinematics in practice.

Force measurements along the lift direction from the sensor belonging to the two trials are shown in figure 8(c)-(d). It can be seen that the measurements reveal that forward and backward strokes are not perfectly symmetrical. This is likely owe to the asymmetric design of the hinge and the wing, and the imperfect fabrication. The asymmetric is difficult to avoid in small flapping-wing robots as seen in other notable prototypes [12], [27], [40]. In addition to the aerodynamic lift, the sensor measurements include the inertial effects from the wing. The measurements, therefore, include higher harmonic components from the inertial terms and the oscillation. Since the stroke-averaged contribution from the inertial terms is zero, the time-averaged data represents the mean lift. For the case without wind, the measurement reveals the existence of a second harmonic element as the major component due to the symmetry between the forward and backward strokes. The presence of higher harmonic components are likely due to the vibration of the robot and the setup. The wind results in an apparent change in the instantaneous force, rendering the difference between the forward and backward strokes more pronounced in figure 8(d) when compared to figure 8(c). The instantaneous force measurements are on the order of 50 mN, considerably larger than the sensor’s uncertainty in ideal operating conditions of 0.3 mN. The instantaneous forces are somewhat larger than the time-averaged values of 11.6 and 14.7 mN. We believe the large oscillations are attributed by

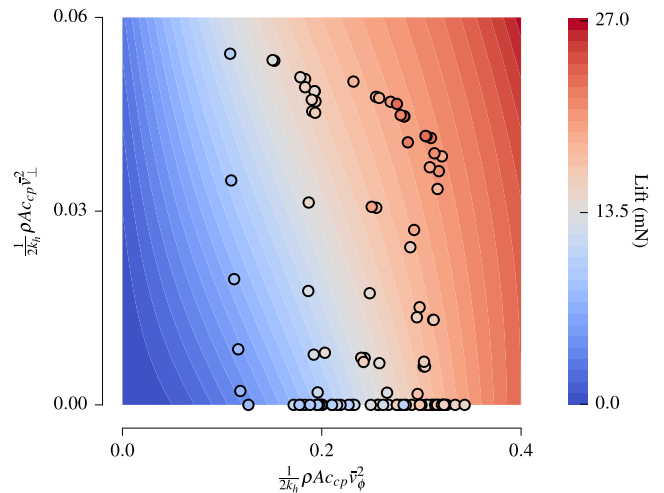


FIGURE 9. Experimental measurements and the aeromechanic model predictions of the stroke-averaged lift plotted against $\frac{1}{2k_h} \rho A c_{cp} v_\phi^2$ (from the measured flapping amplitude) and $\frac{1}{2k_h} \rho A c_{cp} v_\perp^2$ (from the measured flapping amplitudes and frontal wind speed). The color gradient shows the magnitude of the predicted force. The colored circular markers correspond to the experimental data.

the vibration as well as the inertial forces from the motor and the wings. Nevertheless, the observed oscillations should not affect the time-averaged values, which correspond to the lift generated by the robot.

VI. MODEL VERIFICATIONS

A. AEROMECHANIC MODEL

From the measurement of lift and flapping amplitudes, together with the knowledge of the flapping frequency and frontal wind speed, we employ the proposed aeromechanic model given by equation (20) to predict the mean lift and compare the predictions with the measurements. For the model, we assume the c_{cp} of 9.7 mm—the value near the $v_\perp \rightarrow 0$ limit—and the \hat{r} of 0.72, slightly higher than the actual \hat{r}_1 and \hat{r}_2 . As \hat{r}_i is determined solely on the wing shape, the discrepancy may be induced by the imperfect fabrication. In our case, \hat{r} can also be regarded as an empirical quasi-steady model parameter as we do not directly fit lift and drag coefficients (C_{L0}, C_{D0}, C_{D1}) as commonly seen in literature [40], [41]. Relevant model parameters related to the wing and the hinge stiffness are summarized in table 2. The model predictions and experimental results are displayed based on the component corresponding to the speed of the wing ($\frac{1}{2} \rho A c_{cp} v_\phi^2$) and the component corresponding to the external wind ($\frac{1}{2} \rho A c_{cp} v_\perp^2$) as shown in figure 9. Qualitatively, it can be seen that the model predictions are consistent with the measurements. The model accurately predicts an increase in lift at higher wing speed or wind speed. For all 107 data points, the root mean square (RMS) of the prediction errors is 2.0 mN—approximately 14% of the average of all measurements (14.8 mN). The corresponding R-squared value is 0.87.

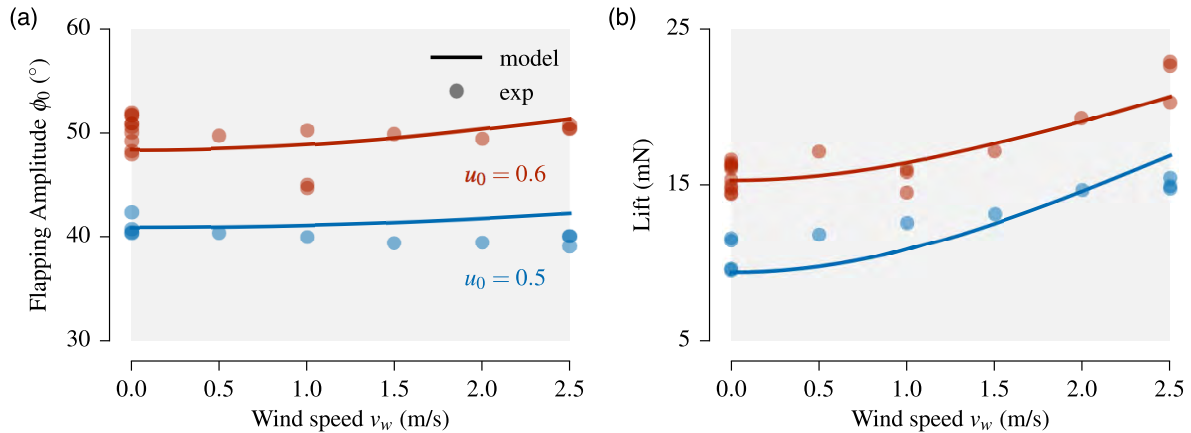


FIGURE 10. Examples of the flapping amplitudes (a) and stroke-averaged lifts (b) from the experimental measurements and the integrated model predictions (without directly using the measurement of flapping amplitudes or wing rotation angles).

B. SYSTEM MODEL

In addition to the stroke-averaged lift, the aeromechanic model developed in Section III-D also provides an expression of the amplitude of the principal component of the drag produced by the flapping wing. Under the assumption that the torque about the flapping axis is proportional to this aerodynamic drag (with r_{cp} being the spanwise center of pressure), the system model equation (25) relates the flapping amplitude (ϕ_0), angular velocity (ω), and wind speed (v_w) directly to the amplitude of the driving signal u_0 . Based on the model parameters identified in Section V-C.1, we re-write equation (25) as

$$\left(\frac{K_s}{K_u} - \frac{J}{K_u}\omega^2\right)\phi_0^2 + \left(\frac{B_1}{K_u}\omega\phi_0 + \frac{r_{cp}}{K_u}\left[\hat{F}_D\right]\right)^2 = u_0^2, \quad (30)$$

leaving r_{cp}/K_u as the only unknown parameter. Using the previous aerodynamic parameters for the calculation of $[\hat{F}_D]$, and through the method of least squares, we find that our model provides a good agreement with the experimental data when $r_{cp}/K_u = 7.93 \text{ N}^{-1}$, capable of predicting the flapping amplitudes from u_0 and v_w with the RMS error of 2.2° . The corresponding R-squared value is 0.95.

To observe the effects of frontal wind on the flapping amplitudes, we inspect the case where the robot was driven at 18 Hz, using the driving amplitude $u_0 = 0.5$ and 0.6 . The plot of measured and predicted flapping amplitudes at different frontal wind speeds is shown in figure 10(a). As anticipated, greater driving signals result in larger flapping amplitudes. The experimental data reveal that the wind speed has minimal effects on the flapping amplitudes, while our model suggests slight changes to the amplitude. Overall, the mismatches between the predictions and the measurements are within a few degrees.

In fact, the subtle changes in the flapping amplitude, according to equation (30), suggest insignificant effects of the wind on the $[\hat{F}_D]$ term. According to the calculation,

the observed amplitudes correspond to $\frac{1}{2}\rho A c_{cp} v_\phi^2 \approx 0.2$ and 0.3 for $u_0 = 0.5$ and 0.6 respectively. As seen in figure 4, our model predicts some reduction in $[\hat{F}_D]$ as the wind speed increases at these conditions. This is consistent with the prediction of a small rise in the flapping amplitude from the system model here. However, the decrease in the drag turns out to be relatively unimportant at the system level in this circumstance, resulting in marginal changes in the flapping amplitude, unobserved in the experimental data. The major reason for this is because our robot exhibits relatively high power dissipation in the linear damping term ($B_1\dot{\phi}$) relative to the nonlinear aerodynamic damping.

C. INTEGRATED MODEL

The system model provides the predictions of the flapping amplitudes from the knowledge of robot's parameters and the driving signals. It follows that we can employ the aeromechanic model to directly predict the stroke-averaged lift from the computed flapping amplitudes, instead of relying on the angle measurements. The integrated strategy potentially simplifies the experimental requirements, allowing researchers to understand the flapping-wing aerodynamics without direct measurements of the flapping amplitudes or wing kinematics of the robots.

Based on the computed flapping amplitude, the aeromechanic model provides the lift force predictions with the RMS error and the corresponding R-squared value of 1.57 mN and 0.90 respectively. The RMS error of the combined method is slightly lower than that of the aeromechanics model alone (1.87 mN). We believe this could be contributed by the inaccurate measurements of the flapping amplitudes as each measurement is achieved using sequence of images from 1-2 flapping cycles only.

Figure 10(b) exemplifies the lift prediction at different wind speeds when the robot was driven at 18 Hz with the driving amplitudes $u_0 = 0.5$ and 0.6 . Both predictions and

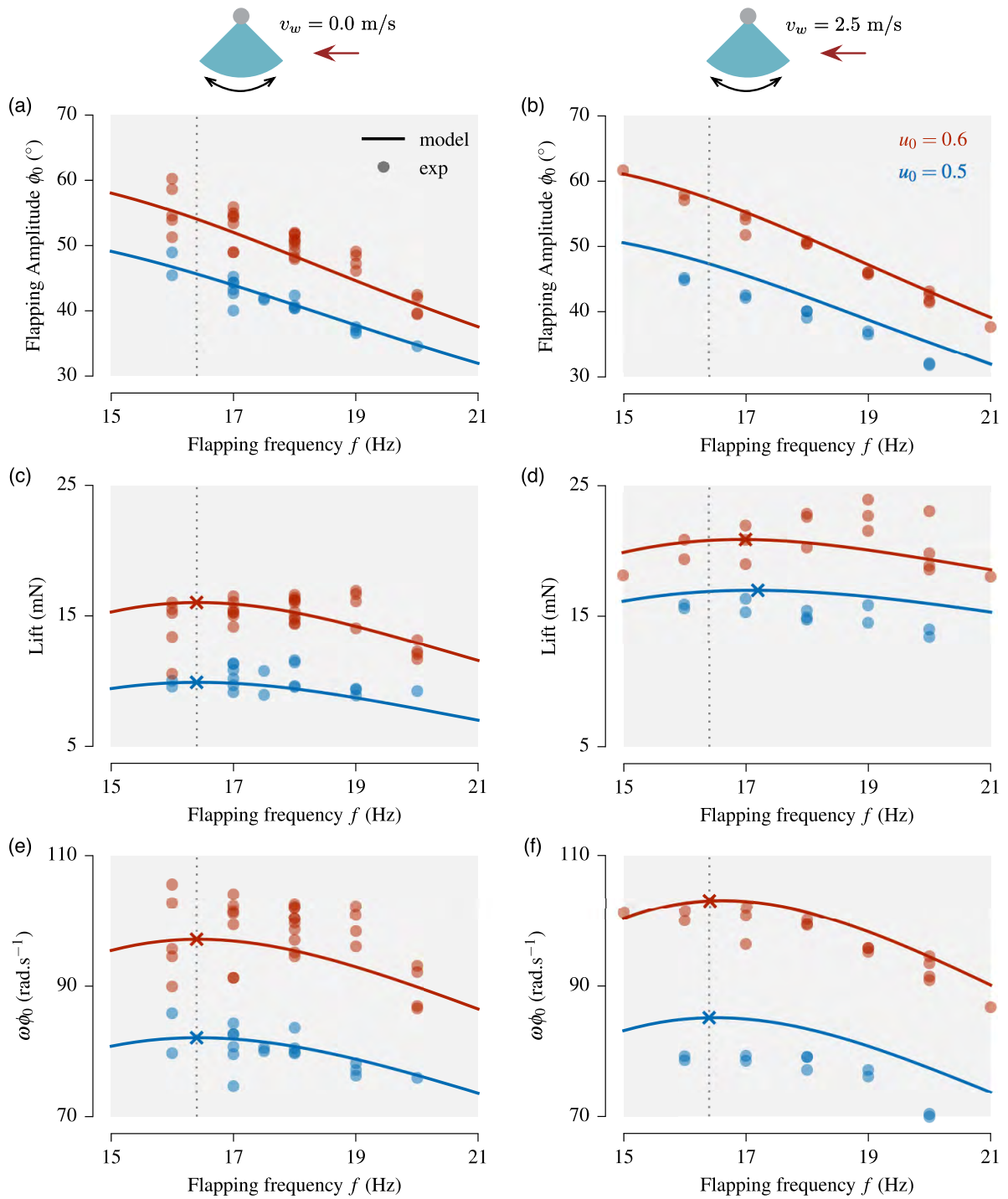


FIGURE 11. Frequency response of the flapping wing robot under two frontal wind speeds. Vertical dotted lines indicate the natural frequency of the system. The crosses mark the anticipated peaks in lift and flapping speed according to the models. (a), (b) the flapping amplitudes as predicted (lines) and measured (dots). (c), (d) the stroke-averaged lifts from the measurements and the integrated model. (e), (f) the flapping speeds from the measurements of ϕ_0 and the model predictions.

measurements reveal a marked increase of up to 40% in lift as the wind speed rises from 0 to 2.5 m/s. The results demonstrate that the frontal wind radically amplifies the lift generated by the robot.

D. NATURAL FREQUENCY ANALYSIS

To see the influence of the flapping frequency on the dynamics of the system, we plot the robot’s flapping amplitude, lift, and the maximum wing speed when the robot was driven at

different frequencies, from 15 to 21 Hz, at two driving amplitudes. The results are shown in figure 11. Two scenarios—no frontal wind and 2.5-m/s frontal wind—were selected to highlight the impact of the frontal wind.

According to the deduced system parameters in table 2, the natural frequency of the robot, where the maximum flapping speed is expected, is 16.4 Hz, independent of the frontal wind speeds. In regular circumstances, the peak frequency, at which the flapping amplitude is maximized, is anticipated to be lower than the natural frequency following the analysis in [9]. Figure 11(a)-(b) displays the measured flapping amplitudes of the robot alongside the predictions from the integrated model. Both show the substantial decrease in flapping amplitude as the flapping frequency rises. It can also be seen that, the measured amplitudes do not vary visibly with the introduction of the wind, whereas the model predicts a slight boost in the flapping amplitudes. However, the discrepancy is not significant. The observation here is consistent with the results in figure 10(a), which shows little changes in the flapping amplitude when the frontal wind is introduced.

Figure 11(e)-(f) illustrates wing speeds from the measurements and the predictions from the integrated model. The model predicts that the wing speed should be highest at the natural frequency (indicated by the dotted lines). With some degree of uncertainty, our measurements follow the predicted course, showing small variation in the flapping speeds near the natural frequency of 16.4 Hz, with a visible roll off at higher frequencies. The trend applies to both driving signal amplitudes, with and without the frontal winds.

Regarding the stroke-averaged lift, our analysis suggests that the natural frequency leads to the maximum lift only when the wind is absent. This is, to some extent, agrees with the observation in figure 11(c). With the 2.5-m/s frontal winds, the combined model indicates that the lift should peak at frequencies higher than the natural frequency, marked by crosses in figure 11(d). The measurements suggest that the lift reaches the maximum at the frequency perceptibly higher than the natural frequency, consistent with the prediction.

VII. CONCLUSION AND DISCUSSION

In this study, we investigate the impact of frontal winds on a flapping-wing robot. The work focuses on a class of small flapping-wing robots that (i) are capable of resonance from the inclusion of a compliant transmission (ii) incorporate passively rotating wing hinges for lift generation. Compared to traditional rigid transmissions, uses of compliant components are increasingly more prevalent in small robots as they reduce the number of parts and lower the actuation requirement [26]. Similarly, the use of flexural wing hinges, which eliminates the need to directly control and actuate the wing rotation, is one of the key techniques that lead to flight capable insect-scale robots [5], [27].

Leveraging the assumption of balanced torque introduced in [29], the angle of attack of a flapping-wing robot with an elastic wing hinge can be approximated in terms of the airspeed. It follows that the lift and drag coefficients for

quasi-steady models, and, subsequently, lift and drag, can essentially be expressed using the airspeed only. This significantly simplifies the analysis. We further propose to write lift and drag coefficients as polynomial functions of the airspeed. As a result, one can analytically evaluate the stroke-averaged lift and the leading harmonic component of drag based on the wing kinematics only. The proposed method also extends to the case of flapping-wing robots facing frontal winds.

The developed aeromechanic method is integrated to the system model. This enables the prediction of lift force directly from the robot's driving signal, bypassing the need to measure the flapping amplitude or the angle of attack. The analysis covers the resonance principles, for describing the response of the system to different driving frequencies.

The experiments were performed on a DC-motor-driven single-wing robotic flapper with a wing semispan of 76 mm. We performed 107 flapping trials using different input signal amplitudes and frequencies, in various frontal wind conditions. Mean lift forces and flapping amplitudes were measured. The flapping conditions corresponded to the intermediate to high Reynolds number ($Re \sim 4 \times 10^4$), while the maximum advance ratio was ~ 0.33 . The results are considered, first, with respect to the proposed aeromechanic model, and, second, to the integrated system model. Overall, the measurements are consistent with the model predictions.

A. EFFECTS OF ADVANCE RATIO

Previously, studies on aerodynamics of flapping wing in forward flight or in the presence of frontal winds commonly rely on the dimensionless quantity, J —the advanced ratio, to quantify the effects of the forward movement in comparison to the reciprocating movement of the wing [18]–[21]. In the listed references, the changes from baseline aerodynamics in lift and drag coefficients (or forces), are described using the notion of the advance ratio.

In our work, we show that, based on the traditional definitions of the quasi-steady models, the contribution from the frontal wind should be expressed in terms of $v_{\perp} = v_w \cos \phi$. While, v_w/v_{ϕ} is directly proportional to the advance ratio, v_{\perp} , alone, is not, as it includes the $\cos \phi$ term. When taking the average of the whole flapping period, the quantity of interest becomes $\bar{v}_{\perp} = v_w J_0(\phi_0)$ as given by equation (17). Our analysis suggests that, for the case of frontal winds, the flapping amplitude is a factor that needs to be taken into account. This is sensible as the wind direction becomes less perpendicular to the wing surface at large flapping angle. It follows that, the rest of this paper uses \bar{v}_{\perp} , not J , to describe the contributions of aerodynamic forces stemmed from the frontal winds. The experiments were also performed on a robot at a range of flapping amplitudes, from 30° to 60° , and the results demonstrate reasonable agreements with the proposed method.

In comparison to a number of previous works that employ J in the analysis for forward flight or frontal winds, our outcomes reinforce, rather than contradict, their results. This is because in each of the listed studies [18], [19], [21], the

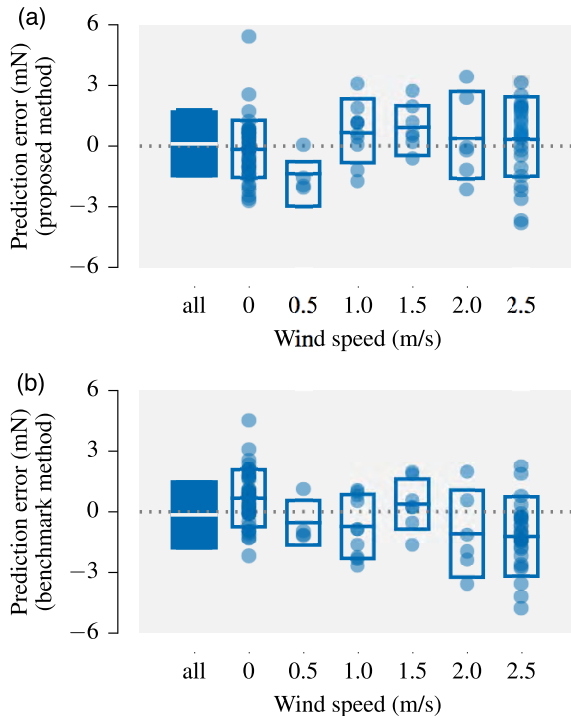


FIGURE 12. Prediction errors of predicted lifts at different frontal wind speeds using (a) the integrated model, and (b) the benchmark model assuming a prescribed wing rotation.

experiments therein were performed at a single, fixed stroke amplitude. This renders the term denoted as \bar{v}_\perp in our work simply proportional to the wind speed. Then, the ratio of \bar{v}_\perp to v_ϕ is proportional to J , making J a valid choice of variable for their respective analysis.

B. COMPARISON TO MODEL WITH PRESCRIBED WING ROTATION

To further evaluate the results, we compare our proposed methods to an existing approach. Traditionally, for a flapping-wing robot with flexural wing hinges, when the measurements of the wing rotation angle are unavailable, researchers often assume that the wing rotation follows some prescribed kinematics. For example, for a sinusoidal flapping trajectory, $\phi(t) = \phi_0 \sin \omega t$, it is reasonable to assume a sinusoidal wing rotation angle $\psi(t) = \frac{1}{2} \psi_0 (1 + \cos 2\omega t)$, with ψ_0 denoting the maximum wing rotation angle. Instantaneous lift force from the flapping motion can be calculated according to equation (6) in the same way regardless whether there exists a frontal wind. This way, however, the wing rotation angle is assumed unaffected by the frontal wind.

To see the lift prediction from this quasi-steady model with a prescribed wing rotation, we calculate the stroke-averaged lift using the flapping amplitude measurements. In this case, we also use a single value of \hat{r} in place of \hat{r}_1 and \hat{r}_2 for consistency with our proposed model. In addition, ψ_0 is treated as another tuning parameter. We find the values of \hat{r} and ψ_0 that minimize the RMS error between the lift

predictions and the experimental results. It turns out that the RMS error from this *benchmark* model is minimized when $\psi_0 = 45^\circ$ and $\hat{r} = 0.72$ (almost identical to 0.73 used for the integrated model). Overall, the resultant RMS error of the lift prediction is 1.63 mN, slightly larger than that of our proposed model (1.57 mN). However, it is important to take into consideration the fact that our integrated model makes the prediction entirely based on the driving signal with only one tuning parameter (\hat{r}), unlike the benchmark model that requires measurements of the flapping amplitude and two tuning parameters (\hat{r} and ψ_0).

To compare the proposed integrated model with the benchmark method more closely, figure 12 shows the prediction errors (the difference between the predicted lifts and measured lifts) from both models, categorized based on different frontal wind speeds. The overlaid boxplots illustrate the mean and the standard deviation of the errors. It is observed the standard deviations from both approaches are comparable. While the overall errors are also similar, the mean errors from the benchmark method tend to be larger than that of the proposed method.

More interestingly, when we calculate the correlation coefficients between the lift prediction errors and the frontal wind speeds, we find that there is insignificant correlation (0.17) from the prediction errors belonging to the integrated model, whereas the errors from the benchmark model result in a moderate negative correlation (-0.49). These correlation coefficients indicate that, the integrated model is equally accurate, irrespective to the wind speed. On the other hand, the benchmark model overestimates the lifts in the absence of wind and underestimates the lifts when there exists strong winds. The moderate correlation of the benchmark model points to the presence of systematic errors. In other words, it suggests that the benchmark model cannot truly capture the effects of the frontal winds and the relatively small RMS errors in the lift estimates are the results of the parameter tuning process. This is unlikely to be the case for our proposed integrated model.

REFERENCES

- [1] D. D. Chin and D. Lentink, "Flapping wing aerodynamics: From insects to vertebrates," *J. Exp. Biol.*, vol. 219, no. 7, pp. 920–932, 2016.
- [2] S. P. Sane, "Neurobiology and biomechanics of flight in miniature insects," *Current Opinion Neurobiol.*, vol. 41, pp. 158–166, Dec. 2016.
- [3] W. Shyy, C.-K. Kang, P. Chirarattananon, S. Ravi, and H. Liu, "Aerodynamics, sensing and control of insect-scale flapping-wing flight," *Proc. R. Soc. Lond. A, Math. Phys. Sci.*, vol. 472, no. 2186, p. 20150712, 2016.
- [4] D. Floreano and R. J. Wood, "Science, technology and the future of small autonomous drones," *Nature*, vol. 521, no. 7553, pp. 460–466, 2015.
- [5] Y. Chen et al., "A biologically inspired, flapping-wing, hybrid aerial-aquatic microrobot," *Sci. Robot.*, vol. 2, no. 11, p. eaao5619, 2017.
- [6] P. Chirarattananon, Y. Chen, E. F. Helbling, K. Y. Ma, R. Cheng, and R. J. Wood, "Dynamics and flight control of a flapping-wing robotic insect in the presence of wind gusts," *Interface Focus*, vol. 7, no. 1, p. 20160080, 2017.
- [7] D. Campolo, M. Azhar, G.-K. Lau, and M. Sitti, "Can DC motors directly drive flapping wings at high frequency and large wing strokes?" *IEEE/ASME Trans. Mechatronics*, vol. 19, no. 1, pp. 109–120, Feb. 2014.
- [8] T. A. Nguyen, H. V. Phan, T. K. L. Au, and H. C. Park, "Experimental study on thrust and power of flapping-wing system based on rack-pinion mechanism," *Bioinspiration Biomimetics*, vol. 11, no. 4, p. 046001, 2016.

- [9] J. Zhang and X. Deng, "Resonance principle for the design of flapping wing micro air vehicles," *IEEE Trans. Robot.*, vol. 33, no. 1, pp. 183–197, Feb. 2017.
- [10] S. Tijmons, G. C. de Croon, B. D. Remes, C. De Wagter, and M. Mulder, "Obstacle avoidance strategy using onboard stereo vision on a flapping wing MAV," *IEEE Trans. Robot.*, vol. 33, no. 4, pp. 858–874, Aug. 2017.
- [11] H. V. Phan, T. Kang, and H. C. Park, "Design and stable flight of a 21?g insect-like tailless flapping wing micro air vehicle with angular rates feedback control," *Bioinspiration Biomimetics*, vol. 12, no. 3, p. 036006, 2017.
- [12] J. Gerdes et al., "Robo raven: A flapping-wing air vehicle with highly compliant and independently controlled wings," *Soft Robot.*, vol. 1, no. 4, pp. 275–288, 2014.
- [13] A. Fisher et al., "The gust-mitigating potential of flapping wings," *Bioinspiration Biomimetics*, vol. 11, no. 4, p. 046010, 2016.
- [14] T. Jakobi et al. (2018). "Bees with attitude: The effect of gusts on flight dynamics." [Online]. Available: <https://arxiv.org/abs/1802.03580>
- [15] H. Wan, H. Dong, and K. Gai, "Computational investigation of cicada aerodynamics in forward flight," *J. Roy. Soc. Interface*, vol. 12, no. 102, p. 20141116, 2015.
- [16] M. Jones and N. K. Yamaleev, "Effect of lateral, downward, and frontal gusts on flapping wing performance," *Comput. Fluids*, vol. 140, pp. 175–190, Nov. 2016.
- [17] C. Zhang, T. L. Hedrick, and R. Mittal, "An integrated study of the aeromechanics of hovering flight in perturbed flows," *AIAA J.*, pp. 1–12, Mar. 2018.
- [18] N. Agre, S. Childress, J. Zhang, and L. Ristroph, "Linear drag law for high-reynolds-number flow past an oscillating body," *Phys. Rev. Fluids*, vol. 1, no. 3, p. 033202, 2016.
- [19] J.-S. Han, J. W. Chang, and J.-H. Han, "The advance ratio effect on the lift augmentations of an insect-like flapping wing in forward flight," *J. Fluid Mech.*, vol. 808, pp. 485–510, Dec. 2016.
- [20] W. B. Dickson and M. H. Dickinson, "The effect of advance ratio on the aerodynamics of revolving wings," *J. Exp. Biol.*, vol. 207, no. 24, pp. 4269–4281, 2004.
- [21] M. J. Elzinga, F. van Breugel, and M. H. Dickinson, "Strategies for the stabilization of longitudinal forward flapping flight revealed using a dynamically-scaled robotic fly," *Bioinspiration Biomimetics*, vol. 9, no. 2, p. 025001, 2014.
- [22] J.-S. Han, J. W. Chang, and J.-H. Han, "An aerodynamic model for insect flapping wings in forward flight," *Bioinspiration Biomimetics*, vol. 12, no. 3, p. 036004, 2017.
- [23] L. Ristroph et al., "Discovering the flight autostabilizer of fruit flies by inducing aerial stumbles," *Proc. Nat. Acad. Sci. USA*, vol. 107, no. 11, pp. 4820–4824, 2010.
- [24] S. B. Fuller, Z. E. Teoh, P. Chirarattananon, N. O. Pérez-Arancibia, J. Greenberg, and R. J. Wood, "Stabilizing air dampers for hovering aerial robotics: Design, insect-scale flight tests, and scaling," *Auto. Robots*, vol. 41, no. 8, pp. 1555–1573, 2017.
- [25] B. M. Finio, N. O. Pérez-Arancibia, and R. J. Wood, "System identification and linear time-invariant modeling of an insect-sized flapping-wing micro air vehicle," in *Proc. IEEE/RSJ Int. Conf. Intell. Robots Syst. (IROS)*, Sep. 2011, pp. 1107–1114.
- [26] C. Zhang and C. Rossi, "A review of compliant transmission mechanisms for bio-inspired flapping-wing micro air vehicles," *Bioinspiration Biomimetics*, vol. 12, no. 2, p. 025005, 2017.
- [27] J. P. Whitney and R. J. Wood, "Aeromechanics of passive rotation in flapping flight," *J. Fluid Mech.*, vol. 660, pp. 197–220, Oct. 2010.
- [28] Y. Chen, N. Gravish, A. L. Desbiens, R. Malka, and R. J. Wood, "Experimental and computational studies of the aerodynamic performance of a flapping and passively rotating insect wing," *J. Fluid Mech.*, vol. 791, pp. 1–33, Mar. 2016.
- [29] N. Gravish and R. J. Wood, "Anomalous yaw torque generation from passively pitching wings," in *Proc. IEEE Int. Conf. Robot. Automat. (ICRA)*, May 2016, pp. 3282–3287.
- [30] Z. Li, S. Suntharasantic, and P. Chirarattananon, "Simplified quasi-steady aeromechanic model for flapping-wing robots with passively rotating hinges," in *Proc. IEEE Int. Conf. Robot. Automat. (ICRA)*, May 2018, pp. 6110–6115.
- [31] K. Y. Ma, P. Chirarattananon, S. B. Fuller, and R. J. Wood, "Controlled flight of a biologically inspired, insect-scale robot," *Science*, vol. 340, no. 6132, pp. 603–607, 2013.
- [32] T. Deora, N. Gundiah, and S. P. Sane, "Mechanics of the thorax in flies," *J. Exp. Biol.*, vol. 220, no. 8, pp. 1382–1395, 2017.
- [33] L. Hines, D. Campolo, and M. Sitti, "Liftoff of a motor-driven, flapping-wing microaerial vehicle capable of resonance," *IEEE Trans. Robot.*, vol. 30, no. 1, pp. 220–232, Feb. 2014.
- [34] H. T. Schlichting and E. A. Truckenbrodt, *Aerodynamics of the Airplane*. New York, NY, USA: McGraw-Hill, 1979.
- [35] S. N. Fry, R. Sayaman, and M. H. Dickinson, "The aerodynamics of free-flight maneuvers in *Drosophila*," *Science*, vol. 300, no. 5618, pp. 495–498, 2003.
- [36] J. Zhang, F. Fei, Z. Tu, and X. Deng, "Design optimization and system integration of robotic hummingbird," in *Proc. IEEE Int. Conf. Robot. Automat. (ICRA)*, May/June 2017, pp. 5422–5428.
- [37] C. P. Ellington, "The aerodynamics of hovering insect flight. II. Morphological parameters," *Philos. Trans. Roy. Soc. London B, Biol. Sci.*, vol. 305, no. 1122, pp. 17–40, 1984.
- [38] X. Deng, L. Schenato, W. C. Wu, and S. S. Sastry, "Flapping flight for biomimetic robotic insects: Part I—System modeling," *IEEE Trans. Robot.*, vol. 22, no. 4, pp. 776–788, Aug. 2006.
- [39] R. Malka, A. L. Desbiens, Y. Chen, and R. J. Wood, "Principles of microscale flexure hinge design for enhanced endurance," in *Proc. IEEE/RSJ Int. Conf. Intell. Robots Syst. (IROS)*, Sep. 2014, pp. 2879–2885.
- [40] J. Zhang, B. Cheng, J. Roll, X. Deng, and B. Yao, "Direct drive of flapping wings under resonance with instantaneous wing trajectory control," in *Proc. IEEE Int. Conf. Robot. Automat.*, May 2013, pp. 4029–4034.
- [41] M. Azhar, D. Campolo, G.-K. Lau, L. L. Hines, and M. Sitti, "Flapping wings via direct-driving by DC motors," in *Proc. IEEE Int. Conf. Robot. Automat.*, May 2013, pp. 1397–1402.



ZHIWEI LI received the B.S. degree in mechanical design and automation from Tianjin University, Tianjin, China, in 2011, and the M.Phil. degree in mechanical and automation engineering from The Chinese University of Hong Kong, Hong Kong, in 2016. She is currently pursuing the Ph.D. degree with the Department of Mechanical and Biomedical Engineering, City University of Hong Kong.



SOMPOL SUNTHARASANTIC received the B.S. and M.S. degrees in electrical engineering from Chulalongkorn University, Bangkok, Thailand, in 2009 and 2011, respectively. He was a Research Assistant with the Department of Mechanical and Biomedical Engineering, City University of Hong Kong, from 2016 to 2017.



SONGNAN BAI received the B.S. degree in mechanical engineering from Xi'an Jiaotong University, Xi'an, China, in 2017. He is currently pursuing the degree with the Department of Mechanical and Biomedical Engineering, City University of Hong Kong.



PAKPONG CHIRARATTANANON (S'12–M'15) received the B.A. degree in natural sciences from the University of Cambridge, U.K., in 2009, and the Ph.D. degree in engineering sciences from Harvard University, Cambridge, MA, USA, in 2014.

He is currently an Assistant Professor with the Department of Mechanical and Biomedical Engineering, City University of Hong Kong, Hong Kong. His research interests include bio-inspired robots, micro air vehicles, and the applications of control in robotic systems.

• • •